energies

MDPI

Article

Characteristics of Gas–Liquid Slug Flow in Honeycomb Microchannel Reactor

Youkai Jiang [1,2,†], Yaheng Zhang [1,†], Jie Zhang [1,2,*] and Zhiyong Tang [1,2,3,4,†]

[1] CAS Key Laboratory of Low-Carbon Conversion Science and Engineering, Shanghai Advanced Research Institute, Chinese Academy of Sciences, Shanghai 201203, China; jiangyoukai2019@sari.ac.cn (Y.J.); zhangyh@sari.ac.cn (Y.Z.); tangzy@sari.ac.cn (Z.T.)
[2] School of Chemical Engineering, University of Chinese Academy of Sciences, Beijing 100049, China
[3] School of Physical Science and Technology, ShanghaiTech University, Shanghai 201210, China
[4] School of Chemistry and Material Science, University of Science and Technology of China, Hefei 230026, China
* Correspondence: zhangjie@sari.ac.cn
† These authors contributed equally to this work.

Abstract: The gas–liquid slug flow characteristics in a novel honeycomb microchannel reactor were investigated numerically and experimentally. Computational fluid dynamics (CFD) modeling was carried out with Comsol finite element software using the phase-field method, and the simulation results were verified by micro-particle image velocimetry (micro-PIV) analysis. The breakups of liquid slugs at the bifurcations of current honeycomb microchannel followed a complex behavior, leading to non-uniformity in each branch. The pressure distribution inside the microreactor was closely related to the phase distribution. The increasing inlet gas velocity increased the gas phase volume fraction, as well as the gas slug length. Higher gas velocity resulted in stronger turbulence of the liquid phase flow field and a deviation of residence time distribution from normal distribution, but it was favorable to even more residence time during the liquid phase. There also exists a secondary flow in the gas–liquid interface. This work reveals the intrinsic intensified effect of honeycomb microchannel, and it provides guidance on future microreactor design for chemical energy conversion.

Keywords: honeycomb microreactor; gas–liquid slug flow; CFD simulation; micro-PIV

Citation: Jiang, Y.; Zhang, Y.; Zhang, J.; Tang, Z. Characteristics of Gas–Liquid Slug Flow in Honeycomb Microchannel Reactor. *Energies* **2022**, *15*, 1465. https://doi.org/10.3390/en15041465

Academic Editor: Dmitry Eskin

Received: 21 January 2022
Accepted: 15 February 2022
Published: 17 February 2022

1. Introduction

Characterized by large specific surface area, short diffusion transmission path and strong controllability, the microreactor can significantly enhance the mass and heat transfer process, providing a clean and safe chemical production environment [1]. Numerous scientists have scrutinized the flow and heat transfer characteristics of different scale types of fluids because of their importance in providing guidance for various industrial applications and chemical reactor designs. Ramzan et al. [2] investigated the mechanical characteristics of the non-Newtonian second grade nanofluid with gyrotactic microorganisms in heat and mass transfer flow. By using the homotopy analysis method and computer-based programming software, the magnetic dipole effect, activation energy, radiation effect and entropy analysis of distinct quantities were explored, and the effects of numerous parameters on the nanofluid temperature, velocity and entropy generation were discussed. Khan et al. [3] also used optimal homotopy analysis method to explore the mechanical aspects of a bio-thermal system. The time-independent three-dimensional flow of Maxwell nanofluid induced by two parallel rotating disks was analyzed, including the heat transfer, nanoparticle concentration, gyrostatic microorganisms with Hall current effect, Arrhenius activation energy and binary chemical reactions.

Moreover, the fluid behavior in the microchannel is affected by the various external operating conditions and design parameters of the microchannel. Turkyilmazoglu [4]

investigated the gas–liquid plug flow in a microchannel exposed to an external magnetic field to supplement the magnetohydrodynamics (MHD) flow experimental data. The effects of magnetic field on hydrodynamic and thermal properties of plug flows in different cross-sectional channels were examined thoroughly. On the other hand, Li [5] studied the effects of the preparation procedures of the Pt/γ-Al_2O_3 catalyst coating, reaction conditions and channel configurations in the microreactor on the catalytic methane combustion reaction performance.

In the microchannel, the flow pattern is laminar, and the mixing process is dominated by mesoscopic viscous deformation and microscopic molecular diffusion. Wiggins et al. [6] used the deformation and motion theory in theoretical mechanics for laminar micromixing process. It was believed that viscous deformation could increase the contact area between fluids and shorten the diffusion distance, thus accelerating diffusion and improving mixing and mass transfer efficiency. Based on this principle, Adamson et al. [7] proposed that the slug flow could reinforce mixing between the liquid, i.e., by introducing an oil or gas phase, such that the aqueous phase formed droplet slug flow, the mixing process could be confined inside the droplets with enhanced radial mixing. The diffusion, mixing, reaction and chemical analysis are controlled by encapsulating the reactants inside the droplets [8]. Compared with reactors in traditional scale, micro-droplets greatly reduce the consumption of reagents, increase significantly the heat and mass transfer performance due to higher specific surface area and also exhibit more uniform residence time distribution of reactants [9,10]. However, the microchannel size is in the micron magnitude, leading to extremely high flow resistance. Consequently, the upper flow rate is limited, making the droplet productivity of the microfluidic device unable to meet the engineering requirements [11]. The bionic network, which can make the flow circulate through multiple branch channels and realize high-throughput micro-flow operation by transporting the materials from point to surface [12–14], can potentially help solve this problem.

As mentioned earlier, the bionic configuration has excellent transport characteristics. Coppens et al. [15] thus proposed the concept of Nature Inspired Chemical Engineering (NICE). Large numbers of studies have shown that the application of bionic structure in chemical reactors can effectively improve the heat and mass transfer efficiency of the system. Yu et al. [16] carried out the numerical and experimental study of the flow and thermodynamic characteristics of the bionic tree channel and found that the tree-shaped microchannel had a higher heat transfer coefficient and lower energy consumption than the straight tube type. Guo et al. [17] proposed an integrated design, in which multichannel mixer, heat exchanger and reactor were combined in microscale. The test results showed that rather impressive mixing could be achieved in the bionic fractal distributor without increasing energy consumption too much. Huang et al. [18] applied the bionic fractal channel design for methanol reforming and found that high methanol conversion rate and hydrogen production rate could be reached.

With a hexagonal topology, the honeycomb structure has the characteristics of a bionic transmission network. It has the shortest fluid flow path for a given area of microchannel reactor [19]. The flow resistance can be effectively reduced in the fluid network in honeycomb structure, leading to a more rational design of transmission network. In addition, the hexagonal unit structure can effectively save the required material for certain strength. Zhang et al. [20] designed a novel honeycomb microreactor for enhancing the conversion of syngas to olefins. The authors discussed the effects of operating conditions on the reaction performance and compared the honeycomb fractal microreactor with the traditional mini-fixed bed and parallel straight microchannel reactor. They found the honeycomb microreactor could improve both the heat and mass transfer significantly, thus enhancing the reaction conversion and yield of desired lower olefins. These results were explained by the higher surface-to-volume ratio in the honeycomb structure, which reinforced the effect of separation and junction and made the fluid in the different channels contact frequently. Zhang et al. [21] found out that the honeycomb reactor enhanced the gas–liquid mass transfer because of its bifurcations, leading to much higher CO_2 absorption rate in

MEA solution as compared to conventional serpentine tubular reactor. Recently, we also found that honeycomb microreactor could greatly enhance the hydroformylation reaction of olefins as compared to conventional stirred reactors, which could be attributed to its enhanced gas–liquid mass transfer [22]. In the honeycomb microreactor, the gas–liquid flow characteristics directly affect the mass transfer efficiency, thereby influencing the gas–liquid reaction performance.

In addition to experimental observation, numerical modeling is also a powerful tool for investigating the flow characteristics in the microchannels. The principle of computational fluid dynamics (CFD) is to use the numerical method to solve the nonlinear simultaneous differential equations of mass, energy, composition and other parameters, and to solve the details of flow, heat transfer, mass transfer, combustion and other processes. Therefore, CFD is a useful method for studying the science and engineering of plug flows in microscale, and the establishment of a mathematical model is very important. Using this tool, Turkyilmazoglu [23,24] investigated the ignition phenomenon of a non-static combustible solid fuel bed under the exposure of a constant incoming heat flux impinging on the solid surface and carried out the thermal analysis of particulate solids and fluids flowing through a moving bed heat exchanger.

However, to the best of our knowledge, most aforementioned research works dealt with the single-phase flow in the bionic microchannels. Though the honeycomb microchannel reactor was reported previously, the gas–liquid flow characteristics of this microreactor still remain unclear. Moreover, most of the reported simulation results of flow behavior in the microreactors were only verified by the empirical formula without quantitative comparison to the actual flow experimental data.

Therefore, in this study, the gas–liquid slug flow in honeycomb microchannel reactor was studied by CFD simulation, as well as micro-particle image velocimetry (micro-PIV) measurement. The phase-field method was applied to track the diffusion interface between gas and liquid in the simulation. The numerical results were verified by micro-PIV system. The effect of increasing inlet gas velocity on phase distribution, pressure drop, pressure distribution and residence time distribution was then analyzed. Having a full understanding of the gas–liquid flow characteristics in the honeycomb microreactor contributes to this research field.

2. Experimental and Numerical Methods

2.1. Micro-PIV Measurement

2.1.1. Flow Field Test Method

In the present study, the micro-PIV (LaVision GmbH, Göttingen, Germany, Flowmaster) was used to measure the instantaneous flow field distribution by the carrier fluid with 2 μm diameter fluorescent polystyrene tracer particles (HyperCyte, Beijing, China). During the measurement, the laser light was transmitted to the microscope through optical fibers, and then tracer particles were illuminated by a Nd:YAG double-cavity laser. The image pairs were recorded by a dual-frame CCD camera (LaVision, Imager SX 4M). Afterward, each recorded image was segmented into small inquiry windows, and then two corresponding inquiry window images in sequence were processed by cross-correlation to obtain the correlation function map of the possible displacement of particles. The coordinates corresponding to the maximum peak value in the correlation function map were the displacements of particles. The time interval of a laser pulse was defined as dt, within which the particle moved a distance of ds. Then, the velocity of the particle in each inquiry window could be obtained as ds/dt. Finally, all displacement vectors of inquiry windows were converted into a complete transient velocity field distribution map.

The micro-PIV images were pre-processed using background subtraction, and spurious vectors in the liquid flow field were removed in the post-processing step. The adaptive multi-pass algorithm was adopted with a final interrogation window size of 16 × 16 px2 and a 50% window overlap (DaVis 10.1, LaVision). The particle concentration was 5.7 × 107 particles per milliliter, resulting in about two particles per interrogation volume.

2.1.2. Flow Field Test Apparatus

Figures 1 and 2a display the honeycomb structure and photo of the microreactor studied in this work, respectively. The microreactor was manufactured by processing the PDMS (polydimethylsiloxane) channel surface, using a template replication method, punching, cutting, plasma bonding with the PET cover surface and, finally, hot baking. The internal honeycomb microchannel presented 1 mm in width and 0.8 mm in depth. It is noted that these sizes were chosen based on the typical data of microchannels in the literature, and they could be further optimized in the future.

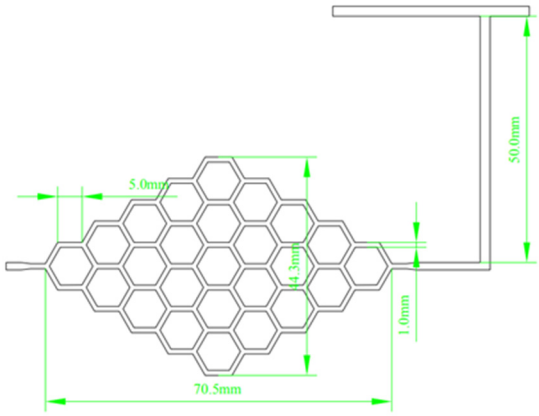

Figure 1. Honeycomb structure of the microreactor used.

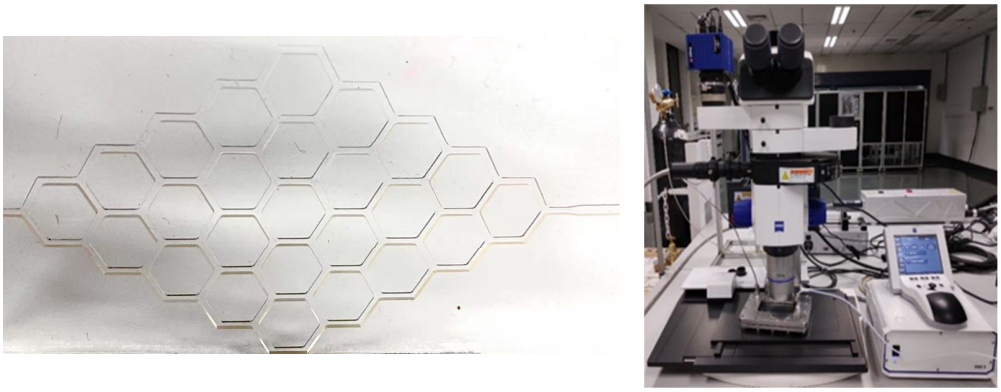

(**a**) (**b**)

Figure 2. (**a**) The photo of honeycomb-shaped reactor; (**b**) Description Micro-PIV photographing platform.

The system diagram of the micro-PIV flow field measurement device is shown in Figure 2b. Nitrogen was used as gas phase, of which the flowrate was regulated from 0 to 10 mL/min by mass flow controller (Beijing SevenStar CS400). Deionized water with tracer particles was used as liquid phase, and its flow rate was controlled by a syringe pump (LongerPump LSP02-1B). The two phases merged at a T-junction before entering the honeycomb microreactor.

2.2. CFD Numerical Simulation

In this study, the phase-field method was used to track the diffusion interface between gas and liquid using COMSOL finite element software, and the two-phase flow dynamics was controlled by Cahn–Hilliard equation. Boundary conditions can be mathematically described as

$$n \cdot \varepsilon^2 \nabla \phi = \varepsilon^2 \cos(\theta_\omega) |\nabla \phi| \, , \; n \times \frac{\gamma^\lambda}{\varepsilon^2} \nabla \varphi = 0 \, . \tag{1}$$

The gas–liquid diffusion interface is defined as the region of dimensionless phase-field variables from −1 to 1. When solving the Cahn–Hilliard equation, it is divided into the following two equations [25]:

$$\frac{\partial \phi}{\partial t} + u \cdot \nabla \phi = \nabla \times \frac{\gamma \lambda}{\varepsilon^2} \nabla \psi \tag{2}$$

$$\psi = -\nabla_\pi \varepsilon^2 \nabla \phi + \left(\phi^2 - 1\right)\phi \tag{3}$$

where u is the fluid velocity (m/s), γ is the mobility ($m^3 \cdot s/kg$), λ is the mixed energy density (N), ψ is the phase-field associated variable and ε (m) is the interface thickness parameter, which can usually be set to $\varepsilon = h_c/2$, where h_c is the characteristic mesh size of the interface area. The mobility parameter γ determines the time scale of the Cahn–Hilliard diffusion. The default value of $\gamma = \varepsilon^2$ is usually a suitable initial setting.

The volume fraction of the fluids can be calculated as follows:

$$V_{f_1} = \frac{1 - \phi}{2},\ V_{f2} = \frac{1 + \phi}{2} \tag{4}$$

In the current model, air was defined as fluid 1 and water was defined as fluid 2. The smoothly varying density (kg/m^3) and viscosity (Pa·s) of the mixture across the two-phase interface are defined by the following expressions:

$$\rho = \rho_w + (\rho_{air} - \rho_w)V_{f1} \tag{5}$$

$$\mu = \mu_w + (\mu_{air} - \mu_w)V_{f1} \tag{6}$$

where the water attribute is represented as w, and the air attribute is expressed as air.

The mass and momentum transfer of fluids were simulated based on the Navier–Stokes equations of incompressible fluids (Equations (7) and (8)), which include surface tension in the model.

$$\rho \frac{\partial u}{\partial t} + \rho(u \cdot \nabla)u = \nabla \cdot \left[-pI + \mu\left(\nabla u + (\nabla u)^T\right)\right] + F_{st} + \rho g \tag{7}$$

$$\nabla \cdot u = 0 \tag{8}$$

where ρ is density (kg/m^3), μ is dynamic viscosity ($N \cdot s/m^2$), p is pressure (Pa), g is gravity vector (m/s^2). F_{st} denotes the surface tension on the air/water interface.

The surface tension was calculated through diffusion interface representation method by calculating the distribution force on the interface and using only the ψ and phase-field variable gradients. This method avoids the use of surface normal vector and surface curvatures, which are difficult to calculate numerically [26].

$$F_{st} = G\nabla\phi \tag{9}$$

where ε is phase-field parameter, G is chemical potential (J/m^3) and can be obtained according to

$$G = \lambda\left[-\nabla^2\phi + \frac{\phi\left(\phi^2 - 1\right)}{\varepsilon^2}\right] = \frac{\lambda}{\varepsilon^2}\psi \tag{10}$$

Different meshes were compared, and the mesh with about 1.2 million structured cells was selected for final modeling, which was also considered for the boundary layer near the wall, since the simulations indicated no significant differences between this mesh and a finer mesh. The boundary conditions were as follows: water was used as the liquid phase, and the liquid inlet speed was 0.01 m/s, while nitrogen was used as the gas phase, and the gas inlet velocity was studied ranging from 0.01 to 0.09 m/s (Condition 1–5) as shown in Table 1; the pressure of the outlet boundary was set as normal atmosphere; the wall

condition was no slip. The initial condition was that the whole channel was full of water phase; then, the two phases entered from the two different inlets and merged to form a slug flow after a T-junction.

Table 1. Conditions of gas velocity.

Condition	1	2	3	4	5	6	7	8	9
Gas velocity (m/s)	0.01	0.02	0.03	0.04	0.05	0.06	0.07	0.08	0.09

3. Results

3.1. Model Verification via Micro-PIV

The statistical results of liquid phase velocity magnitudes of all grid cells in the entire flow channel under operating conditions 3 obtained by simulation calculation and micro-PIV imaging are shown in Figure 3. It can be seen that the statistical results of these two methods were in good accordance. In addition, by capturing a certain liquid column, the velocity curve of the liquid column from the tip to the rear was also analyzed with the simulation and micro-PIV imaging method, as shown in Figure 4. It can be observed that the velocity at the tip was the largest, while the velocity at the interior of the liquid column was relatively lower and uniform in both the simulation and micro-PIV imaging results. Therefore, we can conclude that the characteristics of the slug flow field obtained by micro-PIV imaging were consistent with the simulation results, indicating that the latter were reliable. The discrepancies in Figure 4 could be attributed to the experimental error caused by many experimental factors, such as the wall roughness caused by the microchannel processing technology, the error of PIV measurement, etc.

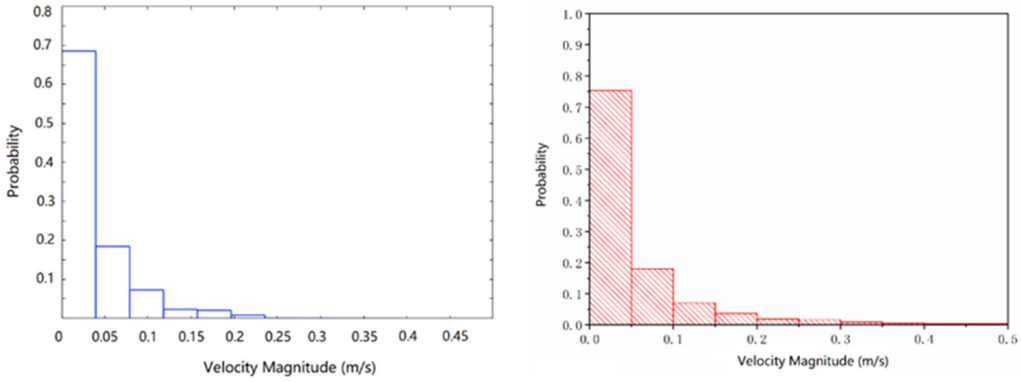

(**a**) (**b**)

Figure 3. Statistical histogram of liquid phase velocity magnitudes of all grid cells under condition 3: (**a**) simulation result; (**b**) micro-PIV experiment result.

3.2. Flow Characteristics Analysis

The phase distribution can intuitively reflect the flow characteristics in the microchannel. Figure 5 shows the volume fraction distribution contour under condition 3. Typical slug flow pattern was observed under the investigated conditions. The overall gas volume fraction in the microreactor increased almost linearly as the inlet gas velocity increased (Figure 6). Moreover, it can be seen from Figure 5 that the splitting of the liquid slug at the bifurcation of the honeycomb microchannel was random. Under the driving force from the upstream fluid, the part of liquid slugs broken up at the bifurcation and the rupture were both symmetrical and asymmetrical, leading to the non-uniformity of flow in each branch of the honeycomb microchannel.

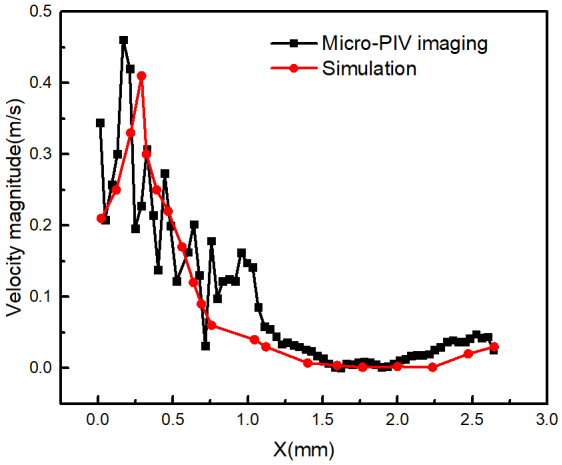

Figure 4. The curve of velocity versus position from the tip to the rear of the liquid column.

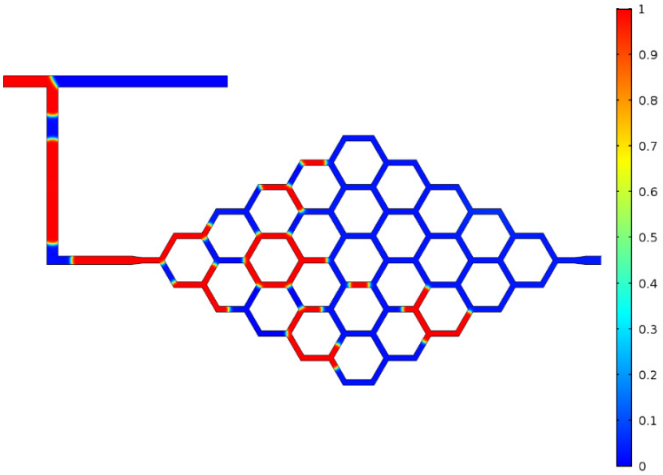

Figure 5. Gas volume fraction distribution contour under condition 3 (t = 7 s).

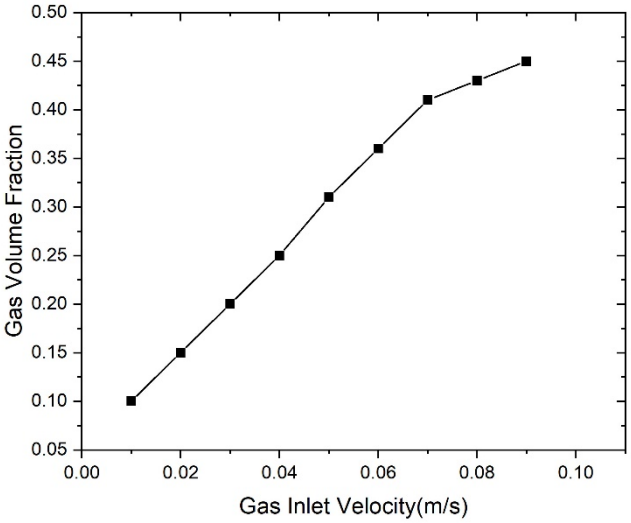

Figure 6. Evaluation of gas holdup fraction as a function of gas inlet velocity.

As illustrated in Figure 7a, the length of the original liquid and gas slug formed after the T-junction was affected by the increasing inlet gas velocity. The original liquid slug length decreased firstly when the inlet gas velocity increased from 0.01 to 0.03 m/s, and it then gradually stabilized at 4 mm when the gas velocity exceeded 0.03 m/s. The original

gas slug length followed a simpler trend, which was almost linearly promoted by the increasing inlet gas velocity. Garstecki et al. [27] proposed an empirical correlation formula to predict the bubble length in T-shaped microchannels. The bubble length was found to be positively correlated with the flux ratio of discrete and continuous phases, which was consistent with our simulation result. Furthermore, it can be seen from Figure 7b that the average liquid slug velocity was considerably favored by the increasing inlet gas velocity in the range of 0.01–0.07 m/s, but it decreased as the inlet gas velocity increased further >0.07 m/s. This can be explained by the fact that the trend of gas shortcut, a phenomenon whereby gaseous fluid flows through the passageway without interacting with the liquid phase, would occur in higher gas velocity conditions, and then, the acceleration to the liquid velocity could be weakened.

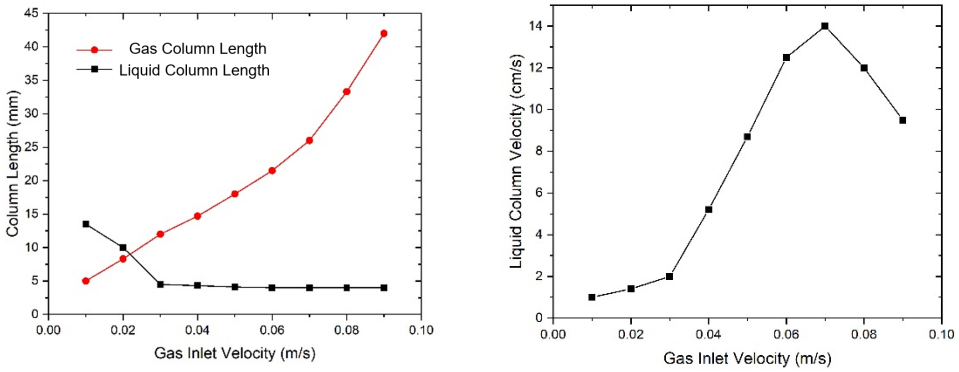

Figure 7. (**a**) Variation of gas and liquid column length with gas velocity conditions; (**b**) Variation of the average liquid column flow velocity with gas velocity conditions.

The liquid slug formation process is a tensile fracture, which is driven by upstream pressure and hindered by the surface tension in the droplet tail region. Figure 8 displays the variation of the overall pressure drops in the honeycomb microchannel with the increasing gas velocity. It can be seen that the pressure drops followed a very similar trend as shown in Figure 7b, indicating that the liquid slug velocity was positively correlated with the change of pressure drop. Consequently, we can conclude that the inertial force dominated during the flow of the liquid slugs, and the effect of surface tension was lower.

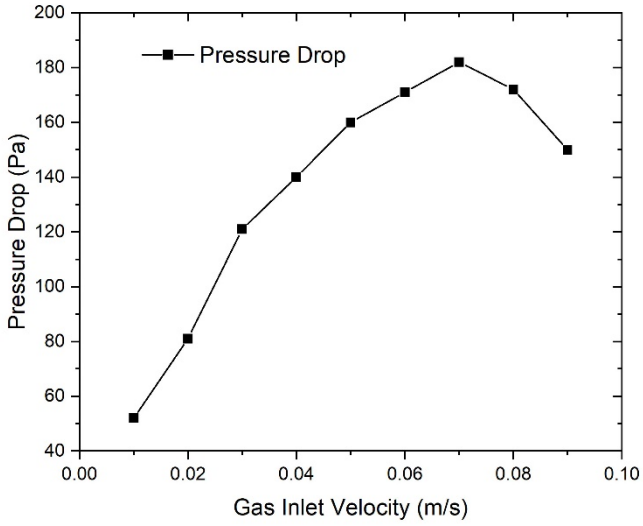

Figure 8. The pressure drop variation of the reactor between the inlet and the outlet with gas velocity conditions.

3.3. Pressure Analysis

The pressure distribution in the honeycomb microchannel under condition 3 can be found in Figure 9a. It was reported that the pressure drop of the gas–liquid flow through the overall arborescence structure increased sharply with the inlet gas flow rate [28]. As for the honeycomb microreactor, the pressure drop increased more slowly, indicating that the design of the microchannel was beneficial for reducing energy consumption. The pressure distribution was closely related to the volume fraction distribution shown in Figure 5. The pressure in the gas phase was higher than that in the liquid phase next to it. Moreover, it can be found that along the direction of gas–liquid flow, the pressures of both the gas and liquid phases decreased, but the pressure drop in the liquid phase seemed more pronounced.

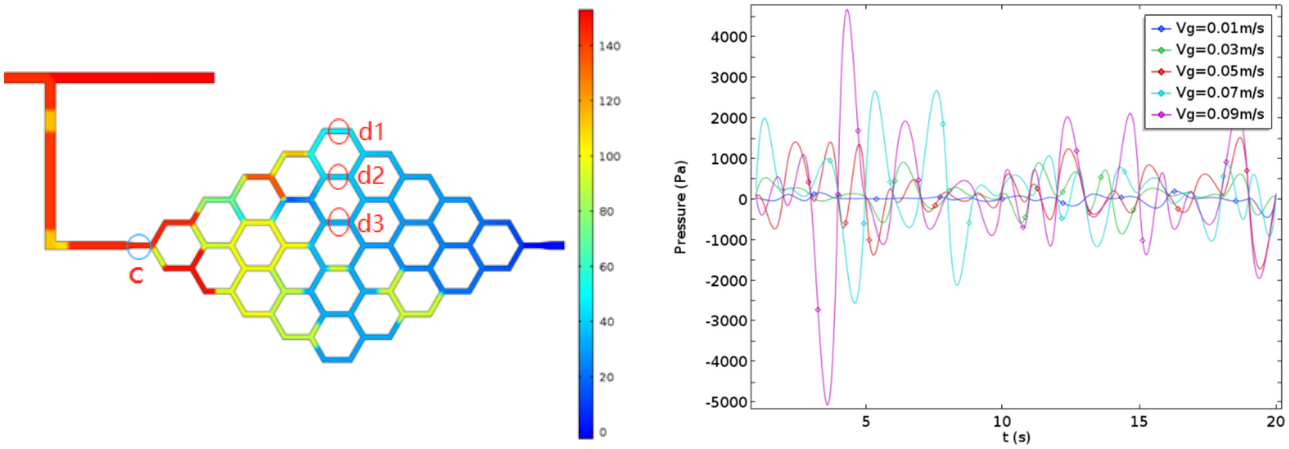

(**a**) (**b**)

Figure 9. (**a**) Pressure distribution contour in the honeycomb microchannel, Pa; (**b**) Pressure fluctuation of point C with time under different working conditions.

The inlet of the honeycomb microreactor was selected as the monitoring point (point c in Figure 9a). Under various inlet gas velocities, the pressure versus time curves are shown in Figure 9b. The fluctuation of pressure became more pronounced with higher gas velocity, but the frequency of pressure fluctuation at each working condition was not affected too much, except with the lowest gas velocity (0.01 m/s). This was consistent with the trend of liquid slug length (Figure 7a), suggesting that the change of pressure along the honeycomb microchannel was mainly influenced by the phase distribution.

The pressure spectrum of the three different branch positions in the honeycomb microreactor (point d1, d2, d3 in Figure 9a) is displayed in Figure 10. It can be seen from the figure that the main frequency of pressure fluctuations for the three monitoring positions was almost the same, reflecting the flow characteristics of different branch flow microchannels exhibiting a certain statistical uniformity for a period of time.

3.4. Residence Time Distribution

By coupling the model of transport of diluted species, the evaluation of the tracer particles' concentration in the liquid phase with the time was simulated in the present work with the purpose to analyze the residence time distribution. Figure 11 shows the concentration of the tracer particles at the exit of the honeycomb microreactor as a function of time under different operating conditions. As the inlet gas velocity increased from 0.03 to 0.09 m/s, the average residence time became just slightly shorter in the honeycomb microchannel, indicating that this honeycomb reactor was suitable for high throughput conditions. Moreover, the residence time distribution under the low inlet gas velocity condition (<0.03 m/s) was approximately the standard normal distribution, which was consistent with that in the straight channel under laminar flow [29]. However, with the increasing inlet gas velocity, multimodal distribution occurred, demonstrating that the

residence time distribution deviated from normal distribution distinctly. It can be explained by the fact that in higher inlet gas velocity conditions, the fracture of liquid columns at the bifurcations is more frequent and random, leading to the distribution of motion paths and residence time of tracer particles showing multimodality. This phenomenon implied that when the gas velocity was higher, the turbulence of the liquid phase flow field was stronger, but the variance of the residence time data would become lower, which was advantageous for practical high throughput flow applications.

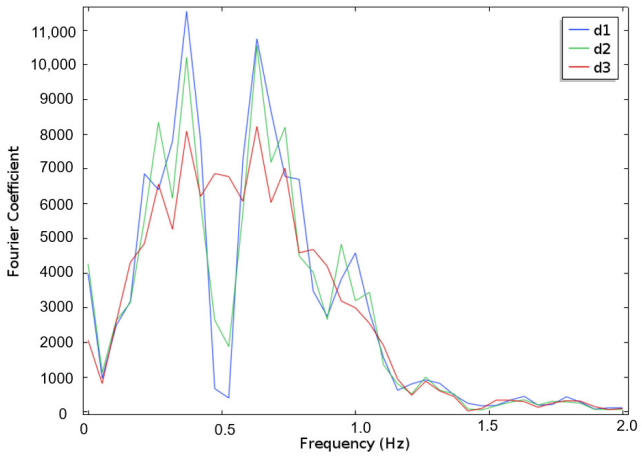

Figure 10. Spectrogram of pressure fluctuations at each branch monitoring point.

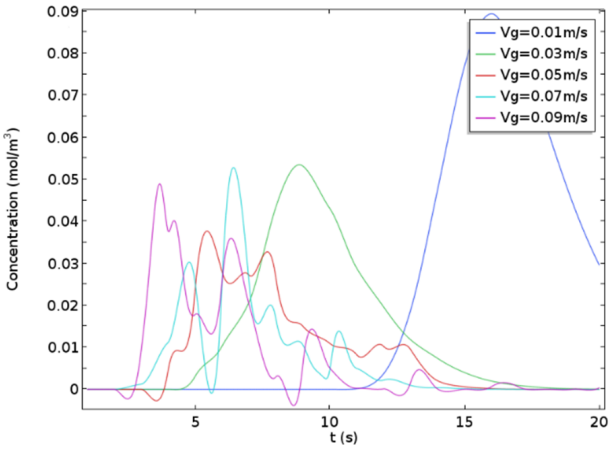

Figure 11. Tracer concentration at the reactor outlet versus time under different working conditions.

3.5. Velocity and Vorticity Distribution

The velocity field distribution under working condition 3 was represented in Figure 12a. At a certain moment, the velocity field distribution in the honeycomb microchannel looked very uneven, and the velocity in the gas–liquid interface changed abruptly. The upstream interface velocity of the liquid slug was maximum, while the downstream interface velocity was almost zero. This could be explained by the fact that the gas phase pressure was greater than the liquid phase in the adjacent region, and the direction of pressure drop at the upstream interface was the same as the flow direction, while the direction of pressure drop at the downstream interface was opposite to the flow direction. Meanwhile, it can be seen from the velocity vector diagram in Figure 12b that a secondary flow formed at the upstream interface of the liquid slug, and a certain velocity component perpendicular to the flow direction was also generated. In addition, the strength of secondary flow was positively correlated with the magnitude of velocity.

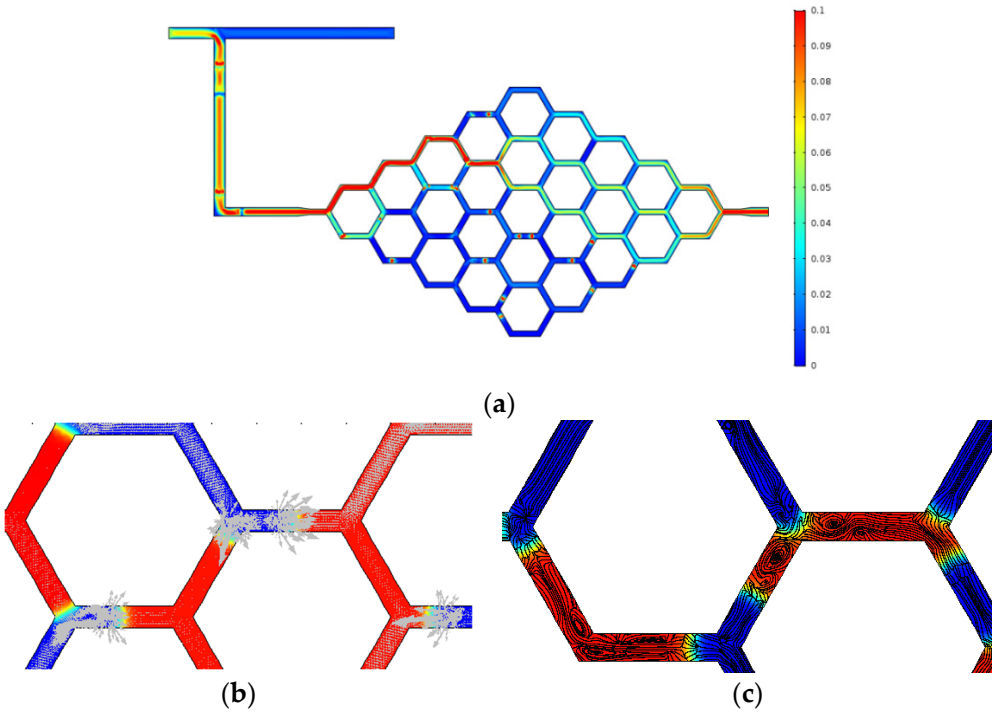

Figure 12. (**a**) Velocity distribution contour under condition 3 (t = 7 s), m/s; (**b**) Velocity vector map under condition 3 (t = 7 s); (**c**) Streamline figure under condition 3 (t = 7 s).

As seen in Figure 12c, vortices appeared in the liquid column, indicating the obvious existence of eddy diffusion. As is known, the mass transfer caused by the intense mixing of vortices is much greater than the molecular motion of laminar flow, for the former is based on particle motion, while the latter is based on the molecular scale. Therefore, the mass transfer rate could be largely enhanced compared to the single-phase laminar flow.

The vorticity field distribution under working condition 3 was shown in Figure 13a. Compared with the phase distribution contours in Figure 5, we can see that a strong vorticity field was formed in the gas–liquid interface region. Furthermore, as Figure 13b exhibited, the average vorticity of the entire flow channel was strengthened with the increase in the inlet gas velocity, but the increasing amplitude decreased gradually, which was caused by the gas shortcut trend when gas velocity is higher. In addition, the average vorticity fluctuated with time, the frequency of which was almost the same as that of slug generation, and the intensity of fluctuation increased with the rise of inlet gas velocity. This indicated that the gas phase created a large disturbance to the liquid phase flow field, which resulted in a strong secondary flow, thereby contributing to the micromixing inside the liquid slug. These results were in good agreement with the reports of Tan et al. [30], Dietrich et al. [31], and Yang et al. [32], wherein the authors found that higher flowrates enhance mass transfer process.

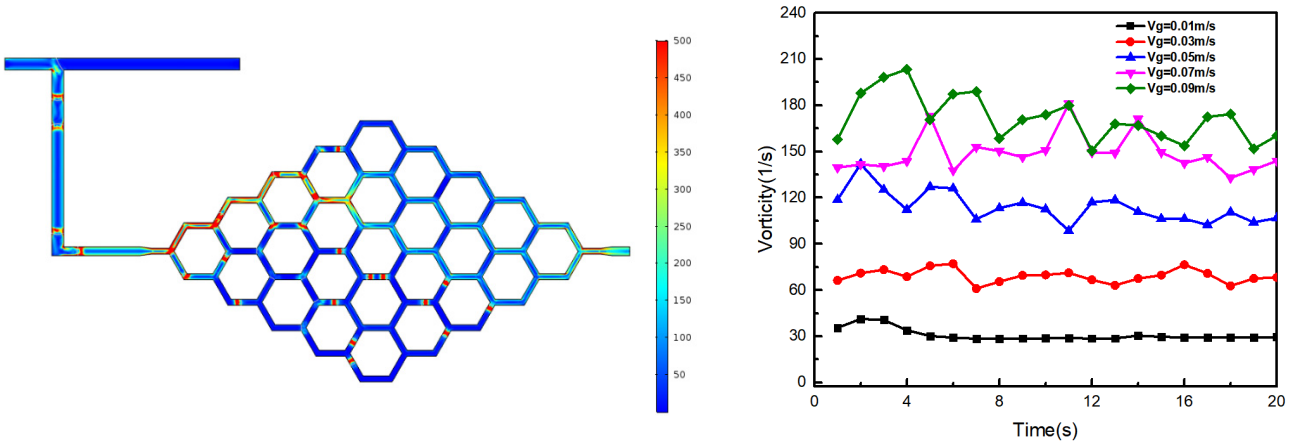

(**a**) (**b**)

Figure 13. (**a**) The vorticity field distribution contour under condition 3 (t = 7 s), s^{-1}; (**b**) The average vorticity with time under different working conditions.

4. Conclusions

In this paper, the fluid dynamics of the gas–liquid slug flow in a honeycomb microreactor was studied by CFD simulation, which was verified by micro-PIV analysis. The present contribution provides detailed analysis of gas–liquid slug flow in honeycomb microreactor, which is helpful for the practical application of this kind of reactor. The following points warrant being highlighted:

- Under current honeycomb configuration, the liquid slug split at the bifurcation randomly, leading to the non-uniformity of the flow in the microreactor. The flow of liquid slug was dominated by the inertial force.
- The pressure distribution was closely related to the phase distribution. The pressure in the gas phase was higher than that in the nearby liquid phase, and it decreased more slowly along the gas–liquid slug path.
- The increasing inlet gas velocity promoted the fluctuation of pressure inside the honeycomb microreactor, but the main fluctuation frequency remained unaffected. With the increasing inlet gas velocity, the gas phase volume fraction and the gas slug length increased, while the liquid slug length decreased.
- Higher inlet gas velocity increased the turbulence in the liquid phase flow field and resulted in the deviation of residence time distribution from normal distribution, leading to a lower variance of the residence time, which was beneficial for practical high throughput applications. In the gas–liquid interface, there was a sudden change of velocity and secondary flow, which was positively correlated with the velocity magnitude, enhancing the micromixing inside the liquid slugs.
- Vortices and eddy diffusion in the liquid columns are favorable for enhancing the mass transfer inside the liquid.

Author Contributions: Conceptualization, J.Z. and Z.T.; methodology, investigation and formal analysis, writing—original draft preparation, Y.J. and Y.Z.; writing—review and editing, supervision, project administration, funding acquisition, J.Z. and Z.T. All authors have read and agreed to the published version of the manuscript.

Funding: This research was funded by National Natural Science Foundation of China (22108288), Youth Innovation Pro-motion Association of Chinese Academy of Sciences and the Key Technical Personnel of Chinese Academy of Sciences, the Ministry of Science and Technology of China and grant number is [2016YFA0602603].

Institutional Review Board Statement: Not applicable.

Informed Consent Statement: Not applicable.

Data Availability Statement: Not applicable.

Acknowledgments: This work was supported by the National Natural Science Foundation of China (22108288), Youth Innovation Promotion Association of Chinese Academy of Sciences and the Key Technical Personnel of Chinese Academy of Sciences, the Ministry of Science and Technology of China (grant 2016YFA0602603).

Conflicts of Interest: The authors declare no conflict of interest.

Nomenclature

u	fluid velocity (m/s)
γ	mobility ($m^3 \cdot s/kg$)
λ	density (N)
ρ	density, (kg/m^3)
μ	dynamic viscosity, ($N \cdot s/m^2$)
p	pressure (Pa)
g	gravity vector (m/s^2)
G	chemical potential (J/m^3)
ψ	phase-field associated variable, (dimensionless)
ε	interface thickness parameter, (dimensionless)
ϕ	phase-field associated variable, (dimensionless)
h_c	characteristic mesh size of the interface area, (dimensionless)
V_{f1}	volume fraction of the air, (dimensionless)
V_{f2}	volume fraction of the water, (dimensionless)
F_{st}	surface tension on the air/water interface, (N/m)

References

1. Jähnisch, K.; Hessel, V.; Löwe, H.; Baerns, M. Chemistry in microstructured reactors. *Angew. Chem. Int. Ed.* **2004**, *43*, 406–446. [CrossRef] [PubMed]
2. Ramzan, M.; Khan, N.S.; Kumam, P. Mechanical analysis of non-Newtonian nanofluid past a thin needle with dipole effect and entropic characteristics. *Sci. Rep.* **2021**, *11*, 19378. [CrossRef] [PubMed]
3. Khan, N.S.; Shah, Q.; Sohail, A.; Kumam, P.; Thounthong, P.; Muhammad, T. Mechanical aspects of Maxwell nanofluid in dynamic system with irreversible analysis. *ZAMM J. Appl. Math. Mech. Z. Für Angew. Math. Und Mech.* **2021**, *101*, e202000212. [CrossRef]
4. Turkyilmazoglu, M. Magnetohydrodynamic Liquid Plug Running in a Micro-Channel: Analytical Solutions. *J. Biomech. Eng.* **2020**, *143*, 011012. [CrossRef] [PubMed]
5. Li, H. Catalytic Methane Combustion in Microreactors. 2020. Available online: https://tel.archives-ouvertes.fr/tel-03022256/document (accessed on 15 January 2022).
6. Wiggins, S.; Ottino, J.M. Foundations of chaotic mixing. *Philos. Trans. R. Soc. London. Ser. A Math. Phys. Eng. Sci.* **2004**, *362*, 937–970. [CrossRef] [PubMed]
7. Adamson, D.N.; Mustafi, D.; Zhang, J.X.J.; Zheng, B.; Ismagilov, R.F. Production of arrays of chemically distinct nanolitre plugs via repeated splitting in microfluidic devices. *Lab Chip* **2006**, *6*, 1178–1186. [CrossRef]
8. Baroud, C.N.; Gallaire, F.; Dangla, R. Dynamics of microfluidic droplets. *Lab Chip* **2010**, *10*, 2032–2045. [CrossRef]
9. Bringer, M.R.; Gerdts, C.J.; Song, H.; Tice, J.D.; Ismagilov, R.F. Microfluidic systems for chemical kinetics that rely on chaotic mixing in droplets. *Philos. Trans. R. Soc. London. Ser. A Math. Phys. Eng. Sci.* **2004**, *362*, 1087–1104. [CrossRef]
10. Manga, M. Dynamics of drops in branched tubes. *J. Fluid Mech.* **1996**, *315*, 105–117. [CrossRef]
11. Vladisavljević, G.T.; Khalid, N.; Neves, M.A.; Kuroiwa, T.; Nakajima, M.; Uemura, K.; Ichikawa, S.; Kobayashi, I. Industrial lab-on-a-chip: Design, applications and scale-up for drug discovery and delivery. *Adv. Drug Deliv. Rev.* **2013**, *65*, 1626–1663. [CrossRef]
12. Conchouso, D.; Castro, D.; Khan, S.A.; Foulds, I.G. Three-dimensional parallelization of microfluidic droplet generators for a litre per hour volume production of single emulsions. *Lab Chip* **2014**, *14*, 3011–3020. [CrossRef] [PubMed]
13. Lim, J.; Caen, O.; Vrignon, J.; Konrad, M.; Taly, V.; Baret, J.-C. Parallelized ultra-high throughput microfluidic emulsifier for multiplex kinetic assays. *Biomicrofluidics* **2015**, *9*, 034101. [CrossRef] [PubMed]
14. Kang, D.K.; Gong, X.; Cho, S.; Kim, J.-Y.; Edel, J.B.; Chang, S.-I.; Choo, J.; Demello, A.J. 3D droplet microfluidic systems for high-throughput biological experimentation. *Anal. Chem.* **2015**, *87*, 10770–10778. [CrossRef] [PubMed]
15. Coppens, M.O. A nature-inspired approach to reactor and catalysis engineering. *Curr. Opin. Chem. Eng.* **2012**, *1*, 281–289. [CrossRef]

16. Yu, X.; Zhang, C.; Teng, J.; Huang, S.-Y.; Jin, S.-P.; Lian, Y.-F.; Cheng, C.-H.; Xu, T.-T.; Chu, J.-C.; Chang, Y.-J.; et al. A study on the hydraulic and thermal characteristics in fractal tree-like microchannels by numerical and experimental methods. *Int. J. Heat Mass Transf.* **2012**, *55*, 7499–7507. [CrossRef]
17. Guo, R.; Fu, T.; Zhu, C.; Yin, Y.; Ma, Y. Hydrodynamics and mass transfer of gas-liquid flow in a tree-shaped parallel microchannel with T-type bifurcations. *Chem. Eng. J.* **2019**, *373*, 1203–1211. [CrossRef]
18. Huang, Y.X.; Jang, J.Y.; Cheng, C.H. Fractal channel design in a micro methanol steam reformer. *Int. J. Hydrogen Energy* **2014**, *39*, 1998–2007. [CrossRef]
19. Liu, H.; Zou, M.Q.; Wang, D.L.; Yang, S.-S.; Liang, M.-C. A honeycomb model for tortuosity of flow path in the leaf venation network. *Int. J. Mod. Phys. C* **2014**, *25*, 1450015. [CrossRef]
20. Zhang, X.; Zhong, L.; Zeng, G.; Gu, Y.; Peng, C.; Yu, F.; Tang, Z.; Sun, Y. Process intensification of honeycomb fractal micro-reactor for the direct production of lower olefins from syngas. *Chem. Eng. J.* **2018**, *351*, 12–21. [CrossRef]
21. Zhang, S.; Lua, Y.; Gu, Y.; Zhang, X.; Sun, J.; Tang, Z. The process intensification of CO_2 absorption in honeycomb fractal reactor fabricated by 3D printer. *Chem. Eng. Processing—Process Intensif.* **2018**, *132*, 42–47. [CrossRef]
22. Wang, S.; Zhang, J.; Peng, F.; Tang, Z.; Sun, Y. Enhanced Hydroformylation in a Continuous Flow Microreactor System. *Ind. Eng. Chem. Res.* **2020**, *59*, 88–98. [CrossRef]
23. Turkyilmazoglu, M. Combustion of a solid fuel material at motion. *Energy* **2020**, *203*, 117837. [CrossRef]
24. Turkyilmazoglu, M. Cooling of Particulate Solids and Fluid in a Moving Bed Heat Exchanger. *J. Heat Transf.* **2019**, *141*, 114501.1–114501.5. [CrossRef]
25. Cahn, J.W.; Hilliard, J.E. Free energy of a nonuniform system. I. Interfacial free energy. *J. Chem. Phys.* **1958**, *28*, 258–267. [CrossRef]
26. Jacqmin, D. Calculation of two-phase Navier–Stokes flows using phase-field modeling. *J. Comput. Phys.* **1999**, *155*, 96–127. [CrossRef]
27. Garstecki, P.; Fuerstman, M.J.; Stone, H.A.; Whitesides, G.M. Formation of droplets and bubbles in a microfluidic T-junction—scaling and mechanism of break-up. *Lab Chip* **2006**, *6*, 437–446. [CrossRef]
28. Hou, J.; Qian, G.; Zhou, X. Gas-liquid mixing in a multi-scale micromixer with arborescence structure. *Chem. Eng. J.* **2011**, *167*, 475–482. [CrossRef]
29. Hornung, C.H.; Mackley, M.R. The measurement and characterization of residence time distributions for laminar liquid flow in plastic microcapillary arrays. *Chem. Eng. Sci.* **2009**, *64*, 3889–3902. [CrossRef]
30. Tan, J.; Lu, Y.C.; Xu, J.H.; Luo, G.S. Mass transfer characteristic in the formation stage of gas–liquid segmented flow in microchannel. *Chem. Eng. J.* **2012**, *185–186*, 314–320. [CrossRef]
31. Dietrich, N.; KLoubière Jimenez, M.; Hébrard, G.; Gourdon, C. A new direct technique for visualizing and measuring gas–liquid mass transfer around bubbles moving in a straight millimetric square channel. *Chem. Eng. Sci.* **2013**, *100*, 172–182. [CrossRef]
32. Yang, L.X.; Dietrich, N.; Loubiere, K.; Gourdon, C.; Hébrard, G. Visualization and characterization of gas-liquid mass transfer around a taylor bubble right after the formation stage in microreactors. *Chem. Eng. Sci.* **2016**, *143*, 364–368. [CrossRef]